Bulletin of the Seismological Society of America, Vol. 93, No. 6, pp. 2664–2684, December 2003

Local Earthquake Wave Propagation through Mississippi Embayment Sediments, Part I: Body-Wave Phases and Local Site Responses

by Charles A. Langston

Abstract *P* and *S* body waves from microearthquakes in the New Madrid Seismic Zone (NMSZ) are investigated at selected sites in an effort to understand wave propagation from future large earthquakes. Earthquake body waveforms display distinctive features that constrain the nature of *P*- and *S*-wave local site responses and wave propagation within the unconsolidated Mississippi embayment sediments. Modeling of the waveforms demonstrates that a near-surface low-velocity zone is characteristic of structure within the upper 60 m of the sedimentary column and produces large *P*- and *S*-wave resonance effects that can be used to infer near-site conditions. Site resonance effects change because of velocity heterogeneity between individual receivers but imply that embayment sediments will substantially amplify ground motions at high frequencies. Site resonance affects *P*- and *S*-wave amplitude spectra and can bias estimates of source and anelastic attenuation parameters. Travel times of observed body-wave phases such as *P*, *PpPhp* (the first *P*-wave reverberation within the entire sedimentary column), *Ps*, *Sp*, *S*, and *SsPhp* can be used to estimate the average wave slownesses and Poisson's ratio within the embayment sediments; an average Poisson's ratio of 0.44 is obtained for the central NMSZ under station PEBM. Detailed *S*-wave velocities are derived for a Nafe–Drake sediment model using acoustic well logs and the travel-time constraints of observed seismic phases. V_p/V_s ratios vary from 5.5 near the surface to approximately 2.4 at the base of the sediments. Use of the well-log data in wave calculations also explains much of the nature of *P*- and *S*-wave coda within the waveforms and shows that 1D heterogeneity is a first-order influence on seismic-wave propagation within the Mississippi embayment.

Introduction

Low-velocity, unconsolidated sediments are generally believed to be a source of hazard in amplifying earthquake ground motions because of the large difference in seismic-wave impedance between the sediments and underlying bedrock (Aki, 1988). It is also a commonly held belief that unconsolidated sediments tend to have high values of anelastic attenuation (Q_p^{-1} and Q_s^{-1}) that can serve to damp out high-frequency ground motions (Seale and Archuleta, 1989; Cramer, 1995; Abercrombie, 1997). The Mississippi embayment area of the central United States contains both a dangerous seismic zone capable of large-magnitude earthquakes (Nuttli, 1973; Johnston and Schweig, 1996) and extensive upper Cretaceous to Recent unconsolidated sediments that locally attain a thickness of over 1 km (Fig. 1). These sediments cover the New Madrid Seismic Zone (NMSZ) and experienced catastrophic liquefaction during the 1811–1812 earthquake sequence forming the world's largest field of sand blows (Johnston and Schweig, 1996).

Because large earthquakes are infrequent in the NMSZ, there is little information on actual wave propagation effects within the embayment sediments and how they would respond during strong ground shaking. Indeed, there are significant gaps in knowledge concerning the shear-wave velocity structure over the full depth range of the sediments, although there has been progress in characterizing shallow velocity structure in the upper 30 m in several areas (discussed later). Studies of seismic-wave attenuation (e.g., Al-Shukri *et al.*, 1988; Al-Shukri and Mitchell, 1990; Chen *et al.*, 1994; Liu *et al.*, 1994) imply very high attenuation of body waves in these thick sediments that could significantly damp out ground motions for frequencies greater than 1 Hz (Langston, 2003). Thus, thick, low-velocity embayment sediments could either significantly amplify or attenuate seismic waves propagating through them, depending on velocity and attenuation parameters and on the frequency band of interest (e.g., Aki, 1988).

In this article, I investigate the propagation of body waves from selected local microearthquakes recorded by the

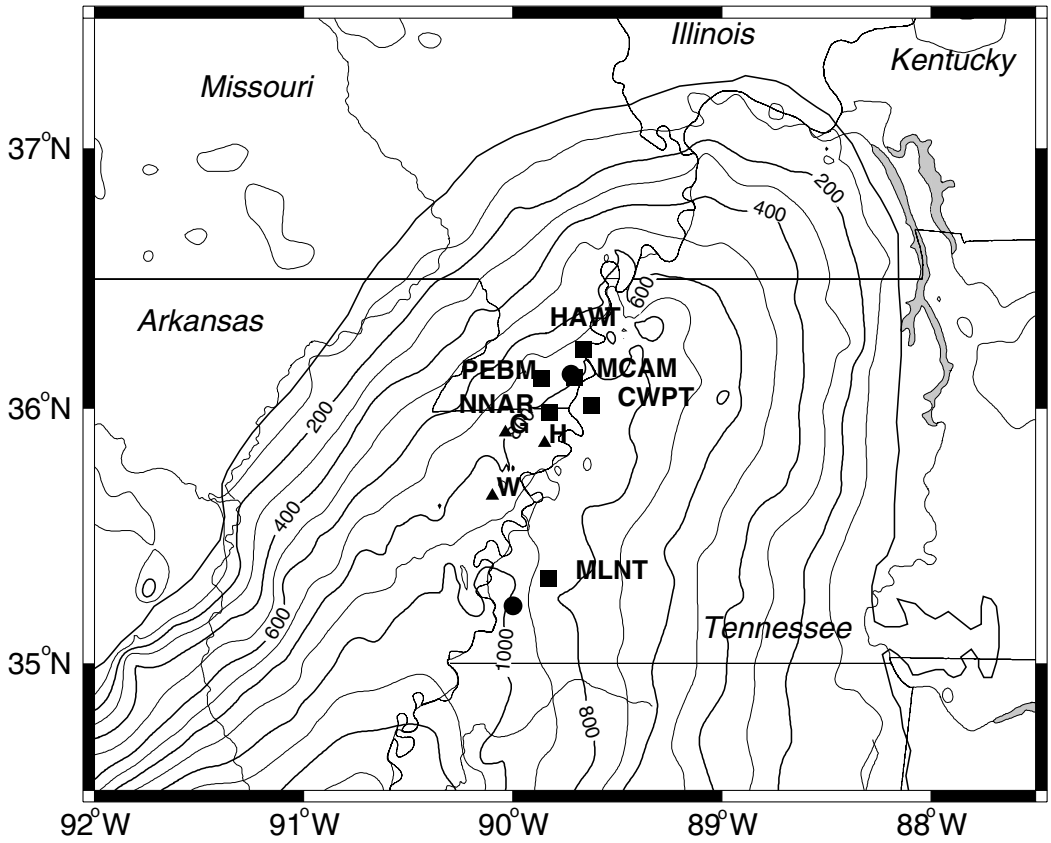

Figure 1. Map showing the study area, stations (squares) used in this study, and earthquakes (circles). Events 1–6 (Table 2) are located nearly below station MCAM. Station parameters are given in Table 1. The triangles show the location of wells from which velocity logs were used in this study (Gao, 1999). G, Dow Chemical/B.L. Garrigan well; H, Amoco Petroleum C./number 1 B.P. Haynes well; W, Dow Chemical/L. Wilson number 1 well. The Wilson 2-14 well is located about 100 m from the Dow Chemical/L. Wilson number 1 well. Also shown are contours of Mississippi embayment sediments taken from Bodin *et al.* (2001).

Center for Earthquake Research and Information (CERI) Cooperative Network to document first-order wave propagation effects and velocity structure in the embayment sedimentary column. The earthquake data proved to be an ideal probe into the character of local site responses and average velocity parameters of the sediments through identification of multiple reflections and primary wave conversions. Results show that the *P* and *S* waves are dominated by profound near-surface low-velocity zones that shape waveforms and amplitude spectra. The data also yield several interesting seismic phases that can be used to estimate bulk properties of the sediments. An average Poisson's ratio of 0.44 is obtained from travel-time analysis of the first *P*-wave reverberation and the *Ps* conversion, yielding the first unambiguous measurement of shear-wave velocity in these sediments. Use of geophysical well-log data from nearby exploratory oil wells gives constraints on the nature of velocity heterogeneity within the sediments and how heterogeneity affects body-wave propagation. More importantly, these wave propagation results have profound implications on the measurement of seismic attenuation from earthquake body waves that are reported in Langston (2003).

Velocity Structure and Anelastic Attenuation in the Mississippi Embayment

The Mississippi embayment is a gentle synform in the central United States filled with up to 2 km of unconsolidated sediments (Fig. 1) (Stearns, 1957; Stearns and Marcher, 1962; Self, 1993). This section of mostly clastic sediments range in age from upper Cretaceous to Eocene with local cover of Neogene sediments associated with the Mississippi River and glacial loess deposits. The northern part of the embayment covers seismicity of the NMSZ and is the location of stations of the CERI Cooperative Seismic Network. The geological character of the embayment is not significantly different than other areas along the southeastern U.S. coast that are covered by unconsolidated coastal sediments. It can be anticipated that results obtained here should

apply to other seismic zones such as near Charleston, South Carolina.

Average crustal velocity structure in the embayment has been investigated by Mooney *et al.* (1983), Ginzberg *et al.* (1983), and Catchings (1999) using seismic refraction techniques and by Nelson and Zhang (1991) using seismic reflection data. In general, the upper kilometer of unconsolidated sediments was not the focus of these studies but deeper geologic structure associated with the Reelfoot Rift Zone (Hildenbrand and Hendricks, 1995).

There have been tomographic studies of earthquake travel times that treat the unconsolidated sediments as a single low-velocity layer (Gao, 1999; Vlahovic *et al.*, 2000). Generally these studies, in conjunction with the refraction results, show the embayment sediments having an average *P*-wave velocity of 1.8–2.0 km/sec. Acoustic well logs are available that show considerable heterogeneity with depth (discussed later) but with average *P*-wave velocities of 1.8–2.5 km/sec within the section. Notably, there have been no direct measurements of *S*-wave velocity over the section, although Liu *et al.* (1997) produced a detailed look of the upper 70 m of the sediment using a vertical seismic profiling (VSP) technique. Also, Dorman and Smalley (1994) estimated the *S*-wave velocity from Rayleigh-wave dispersion from a local earthquake. They obtained an average V_p/V_s ratio of ~3 for embayment sediments.

Recently, there has been considerable effort in characterizing the shear-wave velocity structure of the upper 30 m of the sediments in earthquake hazard analyses. Techniques include use of small-scale seismic reflection and refraction (e.g., Street *et al.*, 2001), small-scale surface wave dispersion (e.g., Romero and Rix, 2001; Rix *et al.*, 2002), and geotechnical cone-penetration tests (e.g., Schneider *et al.*, 2001). These studies uniformly show that shear-wave velocities near the surface are quite low at 150–300 m/sec. Such low near-surface velocities have important implications for estimating earthquake hazards and, for the purposes of this article, help motivate the kinds of models considered in explaining the earthquake *P* and *S* waveform data.

The anelasticity of unconsolidated embayment sediments has been estimated by a number of investigators and is addressed more specifically in Langston (2003). These include earthquake body-wave studies by Al-Shukri *et al.* (1988), Al-Shukri and Mitchell (1990), Liu *et al.* (1994), Cong *et al.* (2000), and Chen *et al.* (1994), a reflection wavefield study by Kang and McMechan (1994), a refracted wave study by Wang *et al.* (1994), and an analysis of VSP *S*-wave data by Pujol *et al.* (2002). In general, those studies that employed high-frequency *P* and *S* waves from local microearthquakes inferred very low values of Q_p and Q_s (10–30). These low *Q*'s have significant implications for expected strong ground motions within the NMSZ. The present study is motivated by an interpretation of local earthquake seismograms recorded at broadband and short-period stations of the CERI network in which it is apparent that very local site conditions affect the waveform of *P* and *S* waves. The working hypothesis of Langston (2003) is that these local site conditions give rise to an elastic wave propagation effect that may bias or influence anelastic *Q* measurements. In seismological practice, the effect of anelasticity depends on how well wave propagation mechanisms are understood. I use the earthquake data to isolate important wave propagation mechanisms and then determine how these wave propagation effects may influence understanding of wave attenuation and amplification.

Microearthquake Data and Data Processing

Figure 1 shows stations utilized in this study. Table 1 lists station locations, and Table 2 lists event parameters for the microearthquake data used here. The CERI Cooperative Network has evolved over the years from an analog short-period network in the late 1970s into a digital, telemetered network in the 1980s. Broadband stations consisting of CMG-40T seismometers started to be included within the network in 1998 by both the University of Memphis and St. Louis University. There are 12 installed broadband stations within the network that record data using 16-bit digitizers. Short-period stations consist mostly of a modified Mark Products L28 three-component seismometer emplaced in shallow boreholes that utilize radio telemetry and modifications of the PANDA I (or ISIS) and PANDA II digitizing systems (Chiu *et al.*, 1991; G. Steiner, personal comm., 2001). Because of the radio telemetry, digital resolution is limited to 12 bits. This relatively low resolution is compensated by a gain-ranging system that allows data from larger events to be amenable to *P*- and *S*-wave travel-time analysis but not for detailed time series analysis since gain ranging is applied before some filtering operations in the telemetry system (G. Steiner, personal comm., 2001). A few stations also contain force-balance accelerometers (Kinemetrics FBA-21) instead of the L28 short-period instrument. All stations sample the ground-motion data at 100 samples/sec. Figure 2 shows the spectral amplitude response of the systems employed in this study.

Although earthquake data from the broadband stations are generally of higher quality, I found that waveform data collected from the short-period stations were quite useful if gain ranging had not been applied to the data stream. This limited the size of events to be less than about magnitude 2.5 (Table 2). A search of the CERI catalog was performed to find microearthquake epicenters located within 20 km of the broadband station PEBM (Fig. 1). The idea was to investigate close-by events in the NMSZ where *P* and *S* waves had not traveled appreciable distances, were simple, and could be described as up-going rays from the source. It can be expected that data for events at relatively large distances will contain a number of differing refracted and reflected paths that would depend on details of deeper crustal structure and would produce complexity in *P* and *S* arrivals (Langston, 1994; Herrmann and Ammon, 1997). It was also important that the waveform data have high signal-to-noise ra-

Table 1
Station Information

Code	Location	Latitude °N	Longitude °W	Depth (m)	Instrumentation
PEBM	Pemiscott Bayou, MO	36.11312	89.86229	2.3	CMG-40T
HAWT	Hathaway, TN	36.2256	89.6596	3	L28/ISIS
MCAM	McCarty, MO	36.1196	89.7024	3	L28/ISIS
NNAR	Number Nine, AR	35.9810	89.8232	3	L28/ISIS
CWPT	Cottonwood Point, TN	36.0091	89.6264	3	L28/ISIS
MLNT	Millington, TN	35.3340	89.8300	0	FBA-21/PANDA II

Table 2
Event Parameters

Event	Date (mm/dd/yy)	Origin Time (UT)	Latitude (°N)	Longitude (°W)	Depth (km)	m_L
1	02/12/00	13:00:09	36.13	89.72	5.5	2.1
2	06/12/00	08:45:47	36.12	89.74	5.1	2.3
3	11/04/00	19:21:47	36.12	89.74	7.6	2.4
4	11/04/00	19:25:08	36.12	89.74	6.1	1.7
5	11/07/00	10:35:35	36.15	89.71	7.8	1.7
6	11/16/00	06:21:20	36.13	89.72	8.2	2.1
7	01/31/01	01:23:55	35.228	89.998	10.7	1.7

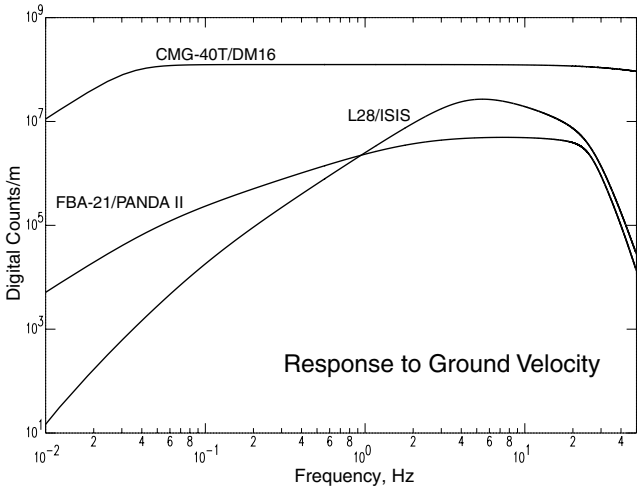

Figure 2. Velocity impulse response for three seismic systems of the CERI network.

tios so that waveform features would be clear and spectra could be computed.

Six events were chosen for study for station PEBM and other short-period stations of the network near PEBM (Table 2). A seventh event was chosen as an event of opportunity since it occurred near the FBA-21 station MLNT and displayed a series of remarkable body-wave phases. These data represent only a very small subset of data that can be studied from the nearly 100 stations of the CERI Cooperative Network. The data and stations were chosen to show the effects of substantially different site structure.

The data (Fig. 3) were corrected using the theoretical system responses for each seismometer to produce displacement waveforms. These displacement waveforms, while containing some long-period noise induced by the instrument correction process, can be interpreted independent of the phase distortions induced by the recording system. In particular, the L28 and FBA-21 systems have very significant phase distortions that mask the character of *P* and *S* waveforms (e.g., see Fig. 3c,d). Instrument corrections were performed using the Seismic Analysis Code (Goldstein and Minner, 1996) function "transfer" and included a frequency domain cosine bandpass window defined by the frequency limits of 0.1, 1, 40, and 50 Hz. Thus, the nominal data bandpass is between 1 and 40 Hz.

Observed Seismic Phases

It has long been recognized that microearthquakes recorded within the NMSZ display distinctive converted phases from *P* and *SV* waves interacting with the unconsolidated sediment–basement boundary (Andrews *et al.*, 1985). Basement rocks consist mostly of the Paleozoic Knoxville Dolomite with *P*- and *S*-wave velocities of approximately 6 and 3.5 km/sec, as determined from refraction interpretations (Mooney *et al.*, 1983; Catchings, 1999), and underlie poorly consolidated upper Cretaceous sediments of the McNairy sand (Crone, 1981; Moore and Brown, 1969) with *P*- and *S*-wave velocities of ~2.5 and ~1.0 km/sec, respectively (discussed later). This interface produces large *P*-to-*SV* and *SV*-to-*P* conversions that are prominent arrivals between the direct *P* and *S* arrivals on seismograms.

Converted phases are commonly observed at nearly every station within the NMSZ and have been the object of study to estimate *S*-wave velocity in the sediments from dif-

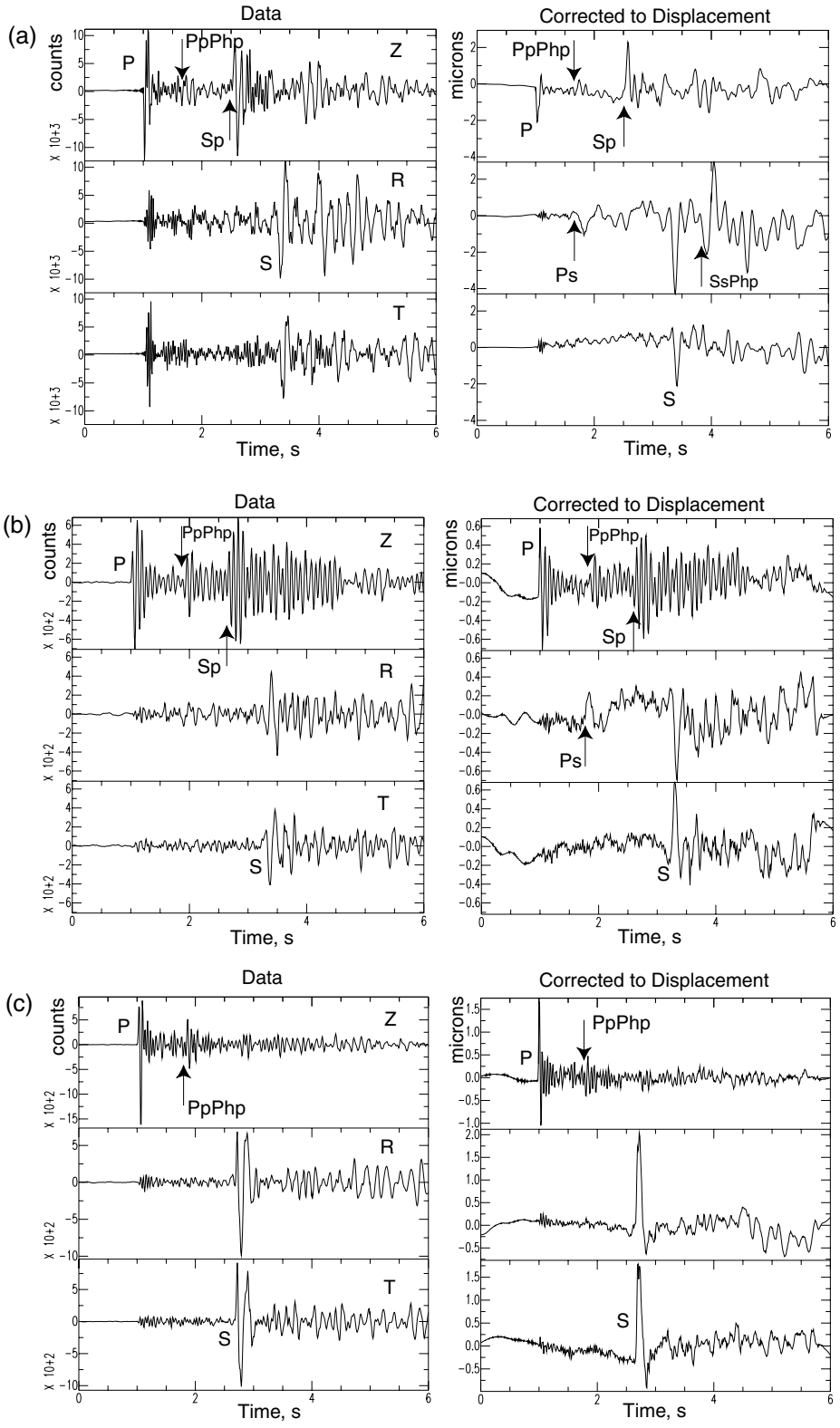

Figure 3. Rotated data (left) and data corrected to ground displacement (right) for events recorded at each seismic station. The horizontal-component data have been rotated into the theoretical radial (R) (away) and tangential (T) (clockwise looking down) directions to separate *P-SV* motions from *SH*. Various seismic phases have been identified and annotated. (a) PEBM station, event 3, (b) HAWT station, event 1, (c) MCAM station, event 5, (d) MLNT station, event 7, (e) CWPT station, event 2, and (f) NNAR station, event 2. (*continued*)

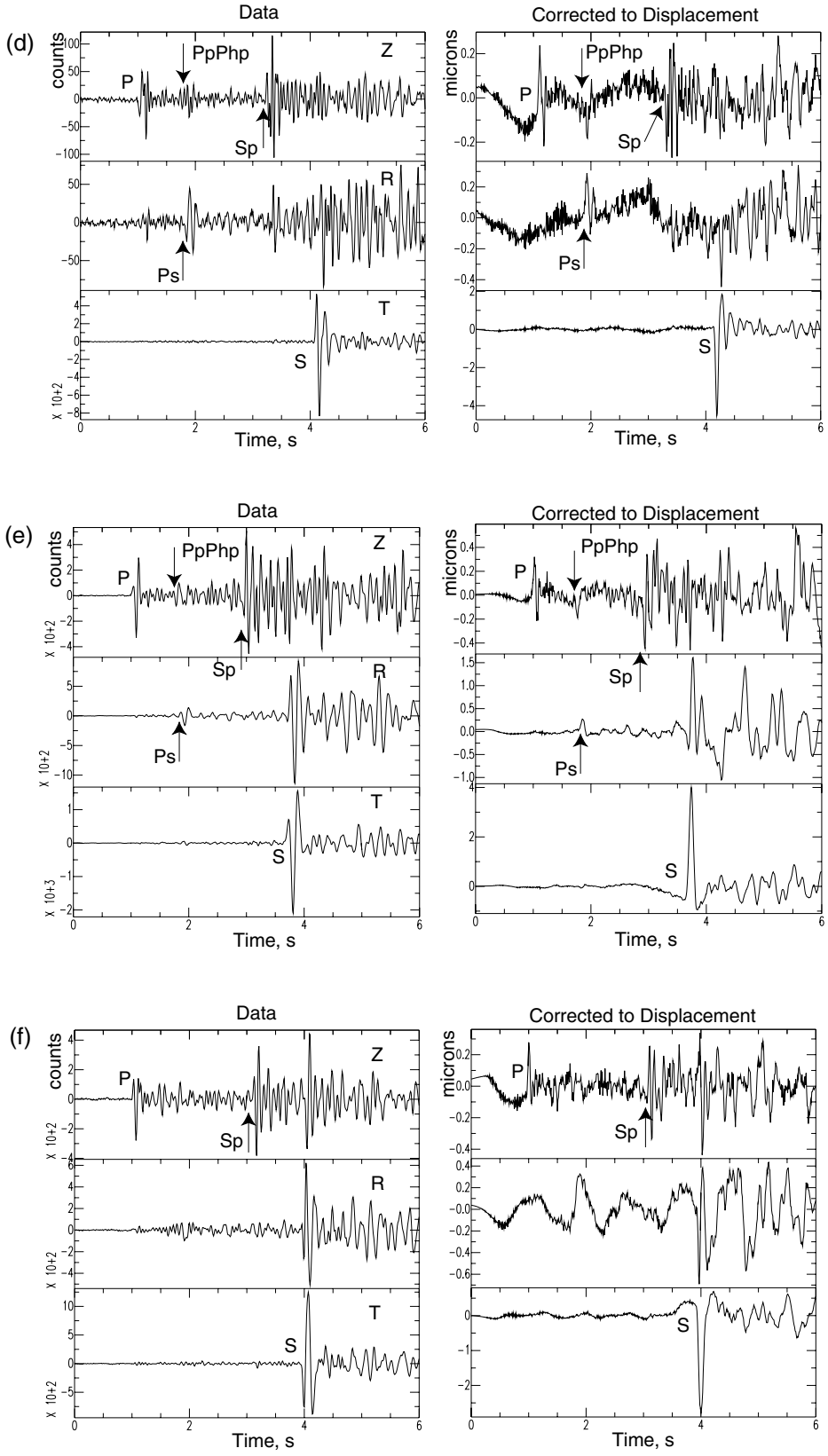

Figure 3. Continued.

ferential travel times (Chen *et al.*, 1996) and to estimate relative attenuation using the *Sp*/*S* spectral ratio technique (Chen *et al.*, 1994). Originally, the large converted phases masked the *S*-wave arrival, particularly when only vertical components were available in the early NMSZ network, and caused problems with event location estimates. The advent of broadband instrumentation within the CERI network allows an unprecedented look into the nature of the wave propagation within the embayment sediments since the data can be more accurately corrected to ground displacement.

Figure 3 shows that the *Sp* phase is a clear arrival on the vertical component in this data set at every station except for, perhaps, MCAM (Fig. 3c). In fact, the low-velocity embayment sediments create a distinctive dichotomy of seismic phases that generally confine *P* waves and *S* waves to the vertical and horizontal components, respectively. Direct *P* is seen on the vertical component at each station with little motion on the horizontal components. Direct *S* generally has very little expression on the vertical component but is very prominent on horizontal components.

Figure 4 and Table 3 illustrate the wave propagation involved with a simple ray diagram for a model that represents embayment sediments as a single layer. A layered velocity model from Chiu *et al.* (1992) was taken to represent structure within the NMSZ (Table 4). This is a modification of the standard model used to locate earthquakes recorded by the CERI Cooperative Network. The sediment layer thickness was varied to investigate any changes in the ray kinematics; results for a 900-m layer thickness and a source depth of 8 km are shown in Figure 4.

P- and *S*-wave rays for earthquakes at a distance of 12 km and depth of 8 km have about the same incident angle of 62° under the sediment layer. *P* and *S* rays in the sediment layer have angles of 16° and 9°, respectively. The observation that there is very little horizontal *P*-wave motion or vertical *S* motion says that the near-surface velocity is considerably less than the velocities assumed in the simple layered model.

Because the sediment layer thickness is relatively small compared to the depth of the earthquakes and because the velocities are so low compared to the wave velocities in deeper regions of the model, there is very little difference in the ray parameters between phases produced by the direct *S* waves (*S*, *Sp*, *SsPhp*) and phases produced by *P* (*P*, *PpPhp*, *Ps*). The phase nomenclature is consistent with Bath and Stefansson (1966), where the first capitalized letter denotes the direct *P* (or *S*), lowercase *p* (or *s*) for a ray propagating upward in the layer, and an uppercase *P* (or *S*) for a ray propagating downward in the layer. The "h" denotes reflection from the base of the layer. Numerical experiments show that the effect of sediment layer thickness on ray parameter is small for these phases and that there are some moderate changes in ray parameter due to source depth, although the primary result of nearly constant ray parameter for individual *P* and *S* phases remains. These results allow a great simplification in the analysis of wave propagation. Synthetic

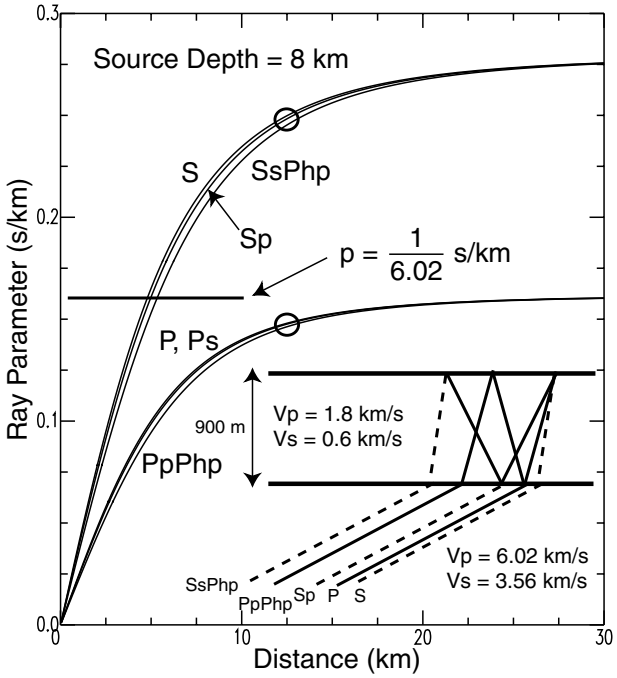

Figure 4. Ray parameter versus distance curve for incident *P* and *S* phases from a source at 8-km depth. Layer parameters are shown in the small inset figure showing ray geometries for each phase of interest. Note that *S, Sp*, and *SsPhp* phases and *P, Ps*, and *PpPhp* phases group closely together, respectively. The two open circles show *P* and *S* ray parameters for event 6 at PEBM. The horizontal line shows the critical ray parameter where *S* phases undergo a phase shift due to a complex transmission coefficient at the basement boundary.

seismograms for *P* and *S* phases will be computed using Thomson–Haskell propagator matrix theory by assuming appropriate ray parameters for incident *P* and *S* waves. Table 3 lists ray parameters assumed in these calculations that were computed using appropriate event depths and distances to each station and the earth model of Table 4.

There is very good consistency in the waveforms of *P*- and *S*-wave trains between earthquakes recorded at station PEBM. Figure 5 shows that the vertical *P*, horizontal *SV*, and *SH* waveforms contain features and arrivals that are common between events. *P* waveforms are most consistent, showing a characteristic waveform and a secondary arrival interpreted through synthetic seismograms (discussed later) as being *PpPhp*. The *Sp* waveforms seem to have more variation and seem to be tied to variation seen in the direct horizontal *SV*. Event 2 (not shown) and event 5 *SV* appeared to be nodal based on the small relative amplitude of these arrivals. *SH* waveforms show similar arrivals within the first 0.75 sec except for event 4 *SH*, which also appears to be nodal. The average (stack) of the normalized waveforms shows the strongest consistent features for each wave train.

A detailed look at *P* and *SH* displacement waveforms from event 2 at PEBM (Fig. 6) demonstrates that there are a

Table 3
Wave Propagation Parameters

Station	Event	Distance (km)	*P*-Wave Ray Parameter (sec/km)	*S*-Wave Ray Parameter (sec/km)
PEBM	2	11.4	0.142	0.242
HAWT	1	11.7	0.142	0.242
MCAM	5	3.1	0.073	0.120
MLNT	7	19.3	0.158	0.267
CWPT	2	15.9	0.150	0.265
NNAR	2	17.5	0.150	0.265

Table 4
CERI Layered Earth Model

V_p (km/sec)	V_s (km/sec)	Density (kg/m^3)	Thickness (km)
1.80	0.6	1890	0.6
6.02	3.562	2700	1.6
4.83	3.20	2500	2.5
6.17	3.57	2700	12.0
6.60	3.82	2800	10.0
7.30	4.22	2900	8.0

number of clear arrivals in the data that are very unlikely to be due to the earthquake source function. The *P* waveform clearly shows a sequence of arrivals each separated by ~0.05 sec that suggests multiple reflections in a shallow layer under the station. The *SH* waveform has a duration about twice that of *P* and also shows at least four arrivals after the interpreted direct *S* separated by ~0.1 sec each. Since these *P* and *S* arrivals are clearly seen in the waveforms of a number of events at PEBM, I conclude that they are due to wave propagation effects of shallow structure under PEBM and not due to an oscillating far-field earthquake source function.

Indeed, it is easy to see that the *P* waveform at each station shown in Figure 3 is quite distinctive from the others, even though all *P* waveforms at PEBM are quite similar. The *P* waveform at HAWT (Fig. 3b) shows a characteristic frequency of oscillation of about 10 Hz, roughly the same as seen at PEBM but with much higher amplitude secondary arrivals. The *P* waveform at MCAM shows a characteristic frequency of 20 Hz, while *P* waveforms at CWPT and NNAR show progressively smaller secondary arrivals, suggesting a more subdued structure response.

The *SH* waves also have a significant range of complexity. The *SH* waveforms for CWPT, NNAR, and MCAM show relatively minor secondary arrivals, while *SH* for PEBM and HAWT have the largest secondary arrivals. *SH* at MLNT (Fig. 3d) shows a regular set of simple apparent reverberations after direct *S*.

Figure 7 shows an example of the spectral signature of the four major arrivals for event 6 at PEBM. The data have not been corrected for the common instrument response, so they are essentially proportional to ground velocity. Each phase and a portion of pre-event noise was windowed using a 1-sec time window and a 5% Hanning taper applied to each end. The amplitude spectra were smoothed with a running average that included three frequency points on each side of the frequency of interest. Pre-event noise amplitude spectra for the vertical, north–south, and east–west components are also shown on the spectral plot. The smoothed spectra show that all phases have similar high-frequency fall-off and levels above 25 Hz. Major differences occur below 25 Hz, where the *S*-wave spectra have prominent peaks near 5 and 20 Hz and a trough at 15 Hz. The *P*-wave spectrum is peaked near 10 Hz, with the *Sp* spectrum containing a broader peak at 15 Hz. According to a simple wave propagation model for the *Sp* conversion, if the *Sp* is due to conversion at the base of the sediments at a first-order velocity discontinuity, then its spectrum should be similar but relatively enriched in high-frequency components relative to the *S*-wave spectrum because of differential attenuation. Clearly, there are major differences in the spectra of *Sp* and *S* that suggest more complex wave propagation mechanisms. The spectrum of *Sp* is most similar to that of *P*, in accordance with a simple look at the vertical data of Figures 3 and 5.

Effect of 1D Heterogeneity in Mississippi Embayment Sediments

How might these data be modeled to determine appropriate wave propagation mechanisms for the *P*- and *S*-wave phases? What constraints on velocity structure are available to place meaningful constraints on these wave propagation mechanisms? The earthquake data displayed in this article are high frequency and suggest that structure with a scale length of $L \sim 0.05$ sec $\times$ 150 m/sec $= 7.5$ m will be important in shaping waveforms and producing multiple arrivals. Clearly, models with a homogeneous embayment sediment layer ~800 m thick will not produce the richness of the observed *P*- and *S*-wave coda.

I approach this problem by making use of acoustic well logs available from oil exploration wells drilled in the embayment. Figure 1 shows the location of four wells that had appropriately detailed acoustic logs to estimate *P*-wave velocity structure. The logs were acquired directly from the well owners and have been studied by a number of investigators to place constraints on the location of the base of the embayment sediments (e.g., VanArsdale and TenBrink, 2000) and to infer average velocity models for earthquake location and tomography purposes (e.g., Gao, 1999). Figure 8 shows a collection of velocity models derived from these logs by modeling each log with 100 layers, with each layer slowness being derived by the average of the acoustic log's *P*-wave slowness over the layer depth range. This method was used for constructing all subsequent models in this article and is equivalent to preserving wave vertical travel time across a region of the model. Additionally, in Figure 8 each model is plotted so that the basement interface occurs at the

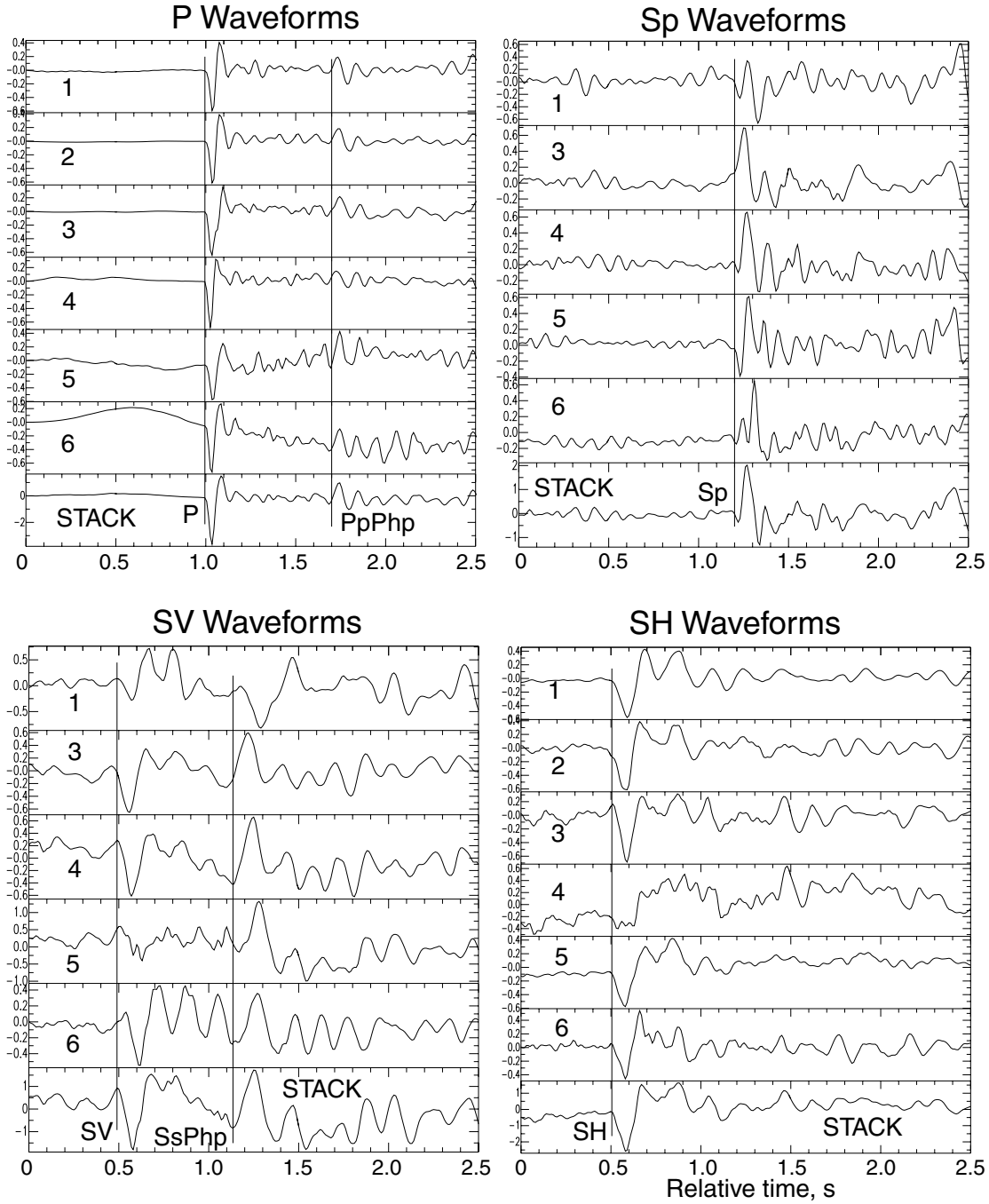

Figure 5. *P*, *Sp*, *SV*, and *SH* waveforms observed from events 1–6 at station PEBM. The displacement data have been normalized and then averaged to produce the stack waveform at the bottom of each panel. Various important seismic phases are annotated.

same depth. This is to examine general trends in the velocity models for similarly aged sediments.

Although there is substantial variability in detail, there is a general similarity in the velocity models when plotted this way in terms of average velocities and trends in velocity gradients, except for the large velocity excursions seen in the Wilson model. These low-velocity excursions were presumably due to borehole washouts in weak muds and do not reflect realistic velocities (P. Bodin, personal comm., 2002). The collection of well-log models shows that there is a general velocity increase with depth to about 500 m, a pronounced low-velocity zone, and then a large velocity increase as the upper Cretaceous sediments are encountered about 200 m above the Paleozoic basement.

The most detailed and, perhaps, reliable well log is the Wilson 2–14 log taken in February 2001, near Kaiser, Ar-

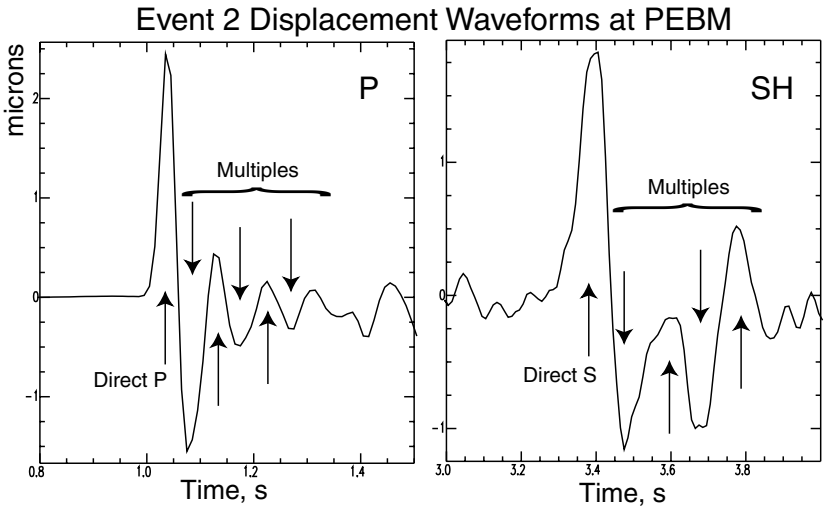

Figure 6. Detail of *P* and *SH* waveforms from event 2 recorded at station PEBM. Arrows show direct arrivals and inferred multiple reflections.

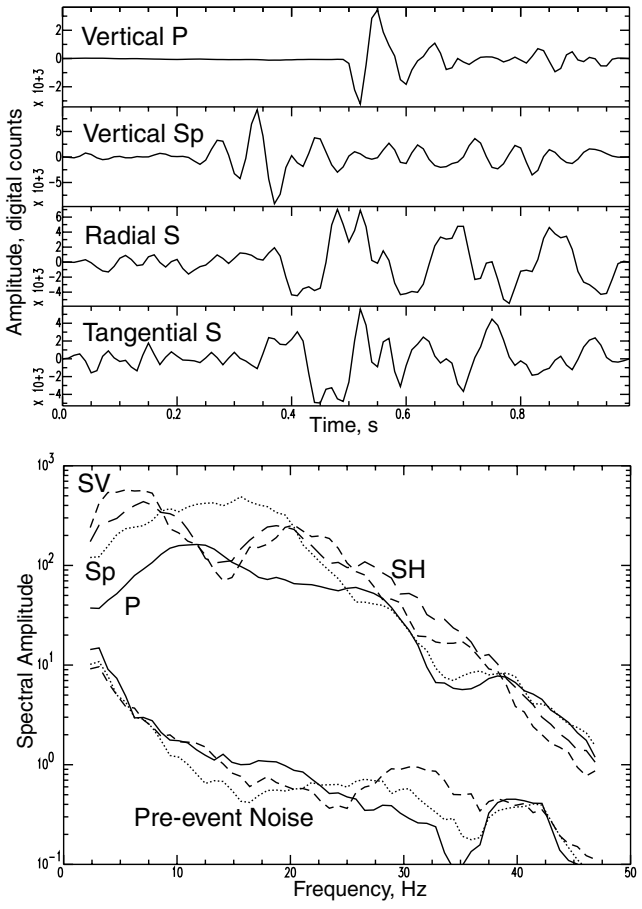

Figure 7. Example of amplitude spectra of the vertical *P*, vertical *Sp*, radial *S*, and tangential *S* waves for event 6 at station PEBM. The windowed, tapered data are shown at the top with amplitude spectra shown below. The spectra have been smoothed using a seven-point averaging operator around each frequency. *Sp* and *P* spectra are similar, as are the *SV* and *SH* spectra. All spectra have similar high-frequency fall-off. Amplitude spectra of pre-event noise are also shown.

kansas (P. Bodin and G. Rix, personal comm., 2001). A representation of the original log is shown in Figure 9. The upper 78 m of the well was cased with steel pipe, so the log is not shown for this depth. The logging tool averaged *P*-wave slowness over 3-ft intervals with a 1-ft depth increment. The velocity variability seen in the log is reasonable and similar to the variability seen in the Garrigan and Haynes velocity logs. It is interesting to note that the large positive excursion seen at about 375 m depth corresponds to an episode of substantial drilling resistance at this depth (P. Bodin, personal comm., 2002). Plane wave synthetic seismograms will be computed for sediment models based on this well log using the slowness averaging method mentioned earlier.

S-wave velocity and density in addition to *P*-wave velocity are required parameters for these computations. However, there are currently no extensive logs in this region for either *S*-wave velocity or bulk density. Dorman and Smalley (1994) suggested a useful empirical approach for deriving both parameters for acoustic velocity logs by using a Nafe–Drake–type sediment model (Nafe and Drake, 1957). Porosity is derived from the observed *P*-wave velocity, an assumed model *P*-wave velocity, water *P*-wave velocity, assumed model density, and water density. Shear-wave velocity is derived from the resulting porosity and assumed model shear-wave velocity. Sediment *P*-wave velocity (V_p) and density (ρ) are assumed to be related to the *P*-wave velocity and density of unbroken, solid model rock (V_{p_s}, ρ_s) and water (V_{p_w}, ρ_w) through the porosity (ϕ):

$$\rho = (1 - \phi)\,\rho_s + \phi\rho_w, \tag{1}$$

$$V_p^2 = \frac{\rho_s}{\rho}(1 - \phi)^5\, V_{p_s}^2 + \phi\left(1 + \frac{\rho_w}{\rho}(1 - \phi)\right)V_{p_w}$$

S-wave velocity (V_s) is related to the porosity and unbroken, model rock *S*-wave velocity (V_{Ss}) through

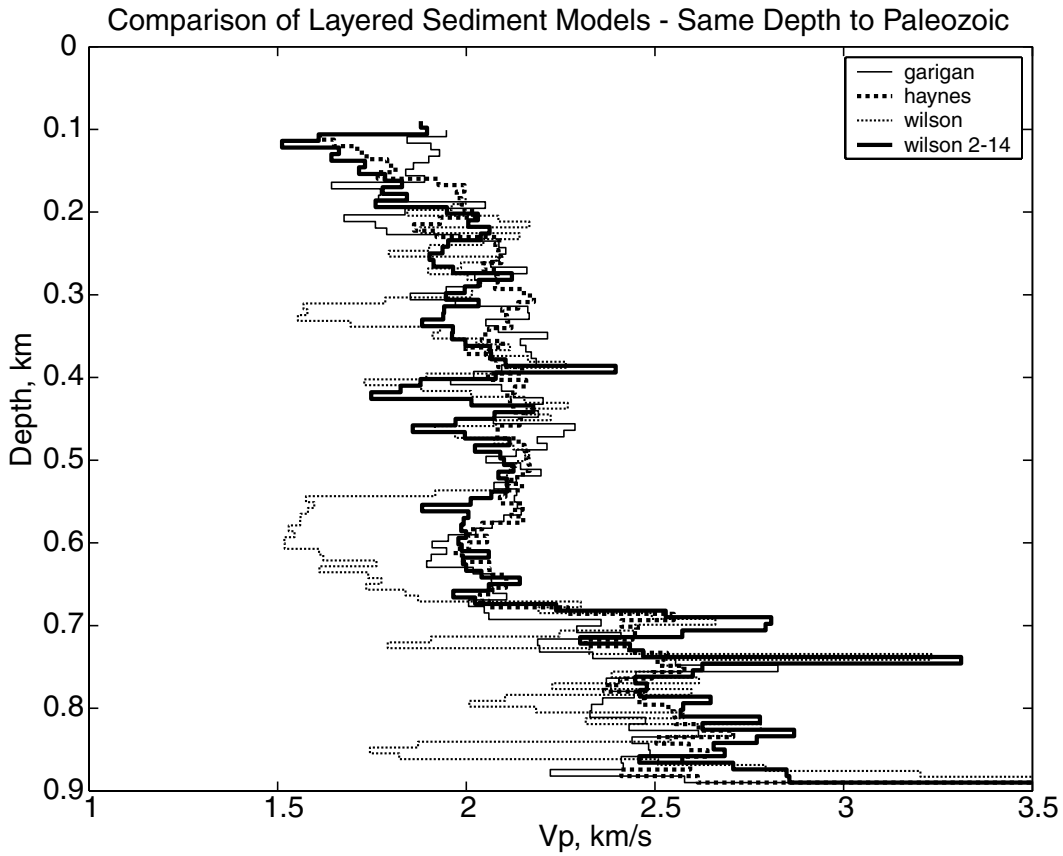

Figure 8. Comparison of layered sediment acoustic velocity models for four different wells. Locations for these wells are shown on Figure 1. The Wilson and Wilson 2-14 wells are within 100 m of each other. The original acoustic velocity logs were processed by averaging slowness over a layer thickness and representing each log by 100 layers. Garigan, Haynes, and Wilson 2-14 models are similar. The Wilson model shows large negative excursions, which are believed to be due to washouts in the well while logging.

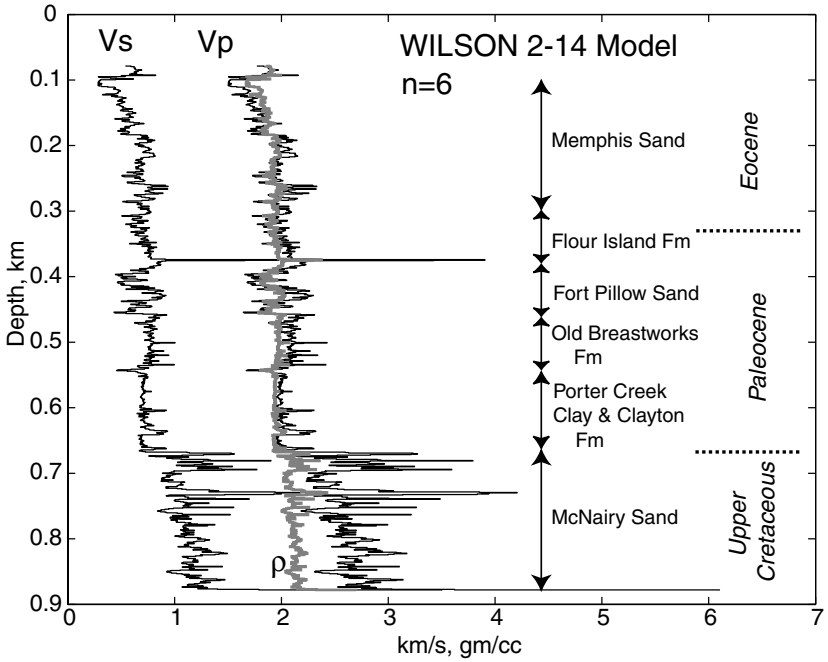

Figure 9. A 1000-layer model derived from the Wilson 2-14 acoustic well log. Porosity, density, and V_s were derived using equations (1) and (2) from the acoustic velocity assuming $n = 6$ in equation (2), $V_{Ss} = 3.5$ km/sec, $V_{Ps} = 6.1$ km/sec, $\rho_s = 2.7$ gm/cc, $V_{Pw} = 1.5$ km/sec, and $\rho_w = 1$ gm/cc. Also shown are formation names and ages taken from Crone (1981) and Moore and Brown (1969).

$$V_S^2 = (1 - \phi)^n V_{S_s}^2. \quad (2)$$

The exponent, n, in equation (2) is the free parameter in this model that must be determined from observations. Nafe and Drake (1957) suggested $n = 5$, and Dorman and Smalley (1994) suggested $n = 6$ for embayment sediments from a surface wave dispersion study. Figure 9 shows the velocity and density functions derived from the acoustic log using $n = 6$. The value of the exponent is investigated below using the travel time of phases through the model.

The major characteristic of the model in Figure 9 is its velocity heterogeneity. The model is not smooth and can be expected to give rise to a complex set of arrivals that should degrade the amplitude and phase of direct arrivals while creating later-arriving coda waves through conversions and multiple reflections. Figure 10a shows the result of a plane wave calculation for incident *P* and *SH* waves under the model of Figure 9. Free-surface displacements are calculated using the Thomson–Haskell technique (Haskell, 1960, 1962) with the addition of anelasticity through complex *P*-wave and *S*-wave velocity (Schwab and Knopoff, 1973; Kind, 1978; Apsel, 1979) using the attenuation model proposed by Futterman (1962) for causal phase:

$$\frac{1}{v_{\text{eff}}} = \frac{1}{v}\left\{1 - \frac{1}{\pi Q}\ln\left(\frac{\gamma\omega}{\omega_0}\right) - \frac{i}{2Q}\right\}, \quad (3)$$

where v_{eff} is the effective *P*- or *S*-wave velocity, Q is Q_p or Q_s, ω is circular frequency, γ is Euler's number, and ω_0 is the low-frequency cutoff for the attenuation band. Sediment velocity structure in Figure 9 was approximated by 1, 10, 100, and 1000 model layers to investigate how layer complexity affects the *P* and *S* waveforms. Q_p and Q_s were assumed be 500 and 250, respectively, for all layers in order to demonstrate elastic wave propagation effects. Ray parameters for station PEBM were taken from Table 3, and the incident wave was constructed to have a simple Brune-model (Brune, 1970) time function with a decay parameter of 0.015 sec. The uncorrupted incident time functions can be seen for the single-layer model in Figure 10a.

The single-layer model shows the usual view of wave propagation in Mississippi embayment sediments. Isolated *P* and *S* waves arrive with a few prominent layer reverberations arriving afterward at relatively late times. As layer complexity increases, the width of the *P* wave changes a small amount, but the *S* wave broadens by a factor of 4 as near-surface reverberations arrive within 0.25 sec of the first arrival. This broadening goes a long way in producing apparent attenuation between the *P* and *S* wave (Langston, 2003). Coda also appears on both the vertical component and tangential component as layer reverberations get larger with greater velocity heterogeneity.

These synthetics suggest that realistic velocity heterogeneity is a prime candidate for producing coda and broadening of *S* waves. However, the synthetics look nothing like the *P*- and *S*-wave earthquake data since there are no clear *P*- or *S*-wave reverberations from the near surface. The well logs are deficient in describing structure near the free surface since each well was cased in this region. Liu *et al.* (1997) provided some valuable insight on the nature of the near-surface structure through VSP logging of shallow boreholes at two sites within the embayment. Figure 11 shows the *P*- and *S*-wave velocity structures determined by these investigators and the expected *P*- and *SV*-wave responses. Each structure shows a very pronounced *P*-wave low-velocity zone that starts at 20 m depth in the Shelby Forest model and at 10 m depth in the Marked Tree model associated with the surface weathering layer and water table. *P*-wave velocities decrease from 1.8–2.0 km/sec to ~250 m/sec or less at the free surface. The *S*-wave velocity undergoes some reduction toward the surface but nothing approaching the changes in the *P*-wave velocity. The *P*-wave response for each model shows that the *P*-wave low-velocity zone produces large near-surface reverberations with fewer effects seen in the *SV*-wave response. (The *SH* response is identical to the *SV* response for all practical purposes.) These effects mimic the character of the earthquake *P*-wave data and also suggest a mechanism for producing reverberations in the *S*-wave data through suitable *S*-wave velocity contrasts near the surface.

Inferred Site Structure

Trial-and-error numerical modeling experiments were performed to fit the timing and amplitude of observed *P* and *S* reverberations seen in the data of Figure 3. The object of the modeling exercise was to determine whether relatively simple velocity structures, for example, a layer, at the top of more complex sediment structure can explain much of the character of the *P* and *SH* waveforms. The primary features of interest in the *P* waveforms include the dominant frequency of the reverberation series and how fast the reverberations decay with time. It is also important that the *S* waves be fit with the same layer model explaining the complexity or lack of complexity in secondary *S* arrivals.

Timing of the reverberations is controlled by the well-known equation for constructive interference of waves in a layer with opposite reflection coefficients at each bounding interface:

$$T = \frac{4D}{v}, \quad (4)$$

where T is the wave period (or time difference between two reverberations in the layer), D is the layer thickness, and v is the wave velocity. Obviously, the observable is T, and the ratio D/v may be constrained but not D or v simultaneously. It might be possible to constrain v by estimating the velocity contrast needed for the decay of the reverberation series, but greater control is needed on velocity in the upper part of the

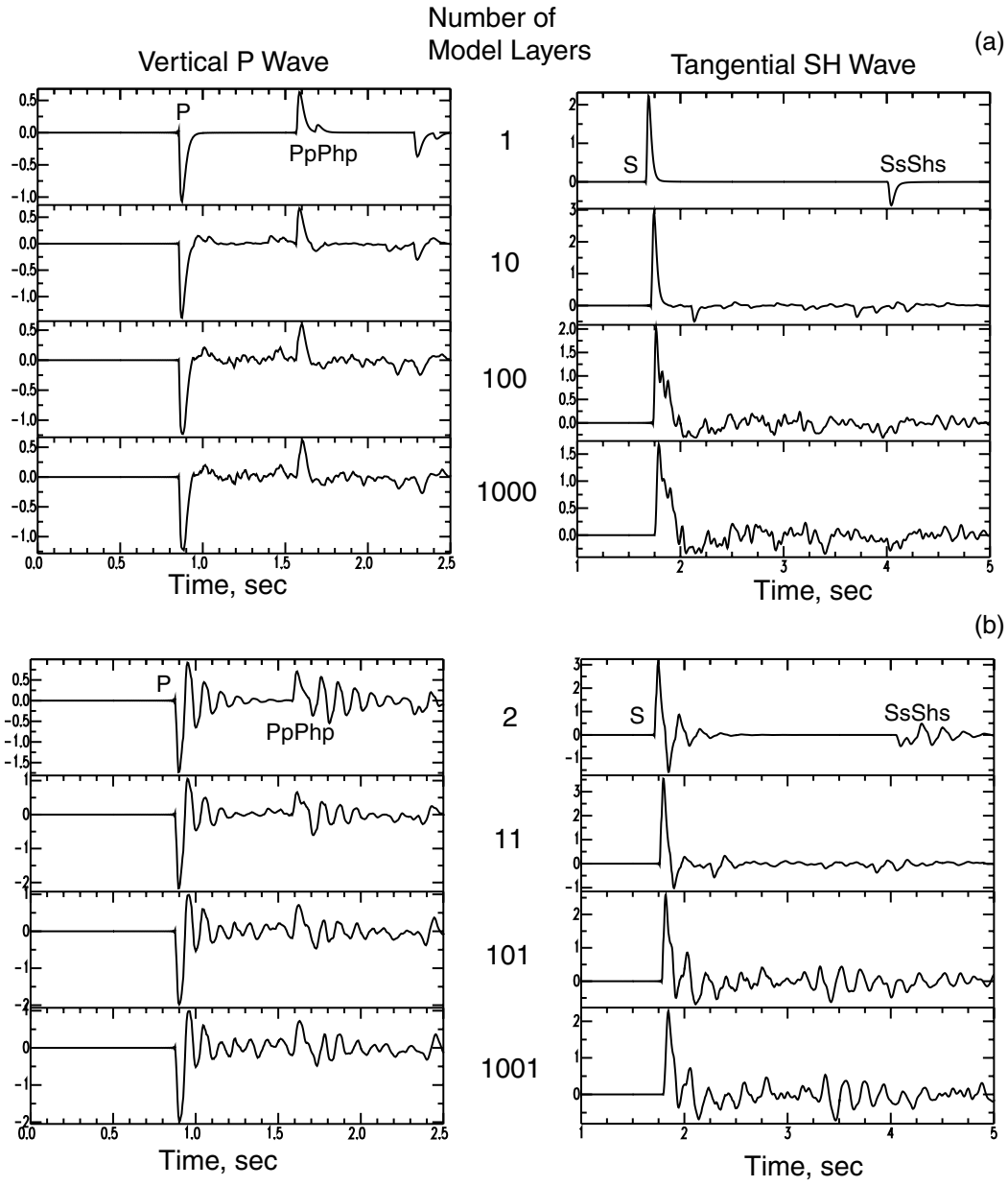

Figure 10. *P*- and *SH*-wave free-surface responses for various layered approximations to the Wilson 2-14 model shown in Figure 9. The number of model layers is shown for each *P*/*SH* response representing how many layers were used to approximate the sediments. The sedimentary column was broken into equal thickness layers, and the average *P*- and *S*-wave slownesses were computed for each layer. *P, PpPhp*, *S*, and *SsShs* phases are annotated. In all cases, note how the *PpPhp* layer reverberation can be seen for increasing heterogeneity but the *SsShs* reverberation quickly degenerates. (a) Responses using the Wilson 2-14 model of Figure 9 without a surface layer. Note how the *S* pulse becomes broad with increasing layer heterogeneity. (b) Responses using the Wilson 2-14 model with a 12.8-m-thick surface layer (PEBM model of Table 5). The *P*-wave response of the surface layer dominates the vertical response, but the *SH* response is more complicated.

sediment column below the low-velocity layer. For example, Figure 11 shows that there are significant variations in velocities between the Shelby Forest and Marked Tree sites. It is also probable that gradients and 1D velocity heterogeneity could be important at individual sites in modeling important waveform details. Another complication involves lack of knowledge of the density profile. The reflectivity of the structure model is a function of acoustic and shear-wave impedances, which involve the product of velocity with density. It is very likely that there are significant density changes

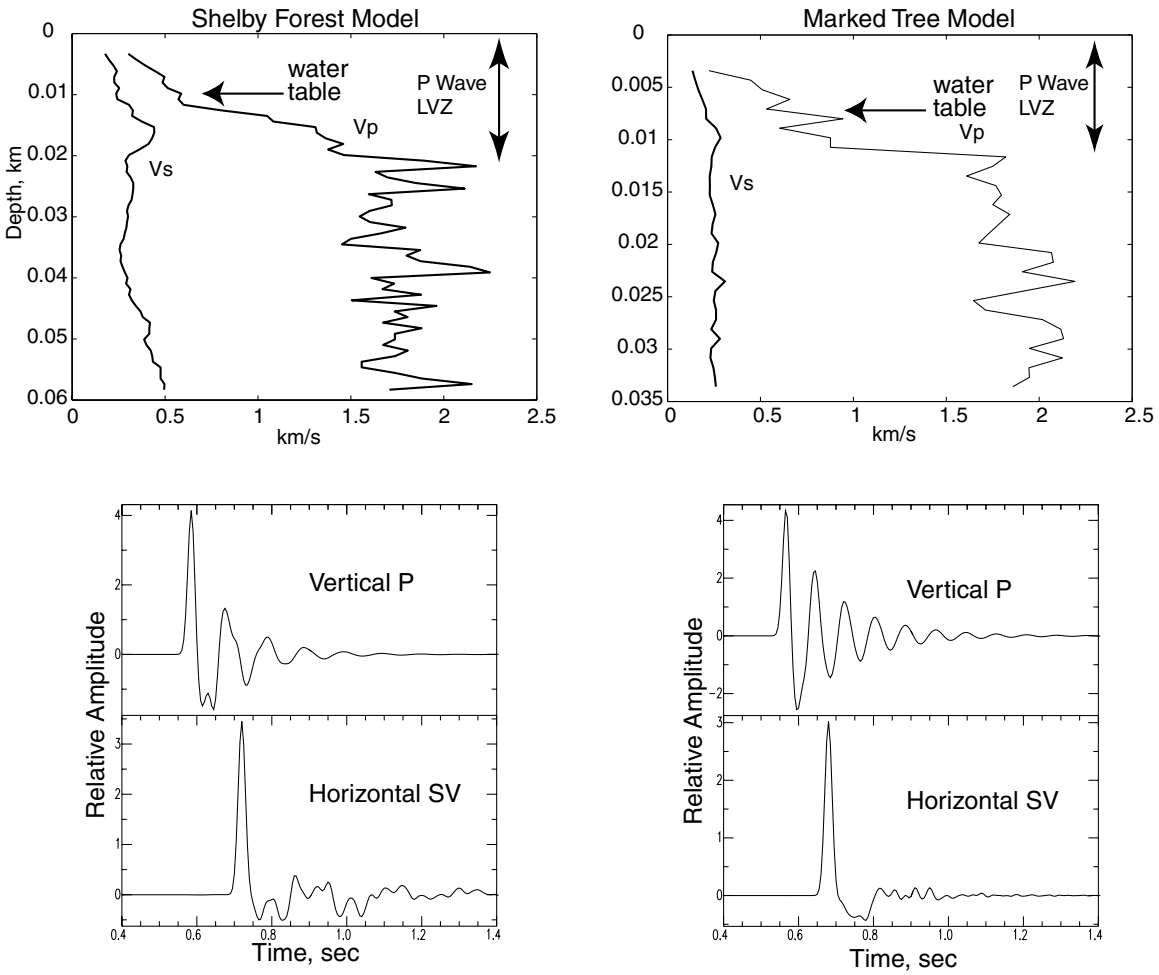

Figure 11. Velocity models obtained by Liu *et al.* (1997) using VSP techniques. The Shelby Forest and Marked Tree sites both show a spectacular near-surface *P*-wave low-velocity zone related to the weathering zone and the water table. The *P*- and *S*-wave responses (below) demonstrate that this kind of structure easily produces clear resonance in the *P* waveforms.

in addition to changes in velocity. Unfortunately, there are no shallow borehole data that report density variations. Nevertheless, simple models were constructed to explore the plausibility of near-surface velocity heterogeneity in controlling *P* and *S* waveforms.

Figure 12 shows the comparison of data and synthetics for the six stations. Table 5 lists the parameters used for the near-surface velocity models inferred from the modeling.

PEBM Structure

PEBM *P* and *SH* waveforms could be modeled using a 13-m surface layer over the Wilson 2-14 velocity model. According to the contours of embayment sediments (Fig. 1), PEBM should be located on sediments ~750 m thick. Although the Wilson 2-14 well penetrated Paleozoic bedrock at 878 m, the model actually starts at 78 m depth due to the well casing problem. Thus, the PEBM model is 813 m thick with the inferred near-surface layer. The model accurately predicts the arrival of the first whole-sediment *P*-wave multiple, *PpPhp*, however. Rather than decreasing the average *P*-wave velocity of the Wilson 2-14 model a small amount while simultaneously decreasing the overall thickness by 63 m, I chose to keep the velocity model intact and simply added the near-surface layer at PEBM. This seemed most prudent because the embayment sediment model of Figure 1 is based on a number of assumptions about *P*-wave velocities in the sediments using oil industry reflection data and only sparse well control (Bodin *et al.*, 2001).

A 13-m layer has a profound effect on the *P*-wave response and fits the timing and relative amplitude of major arrivals in the *P* and *SH* waveforms (Fig. 12). It is interesting to examine the effect of the near-surface layer on the overall response of the Wilson 2-14 velocity model. Figure 10b shows that the vertical *P*-wave response is dominated by reverberations in the near-surface layer. Increasing the number of layers to approximate the Wilson 2-14 well log adds

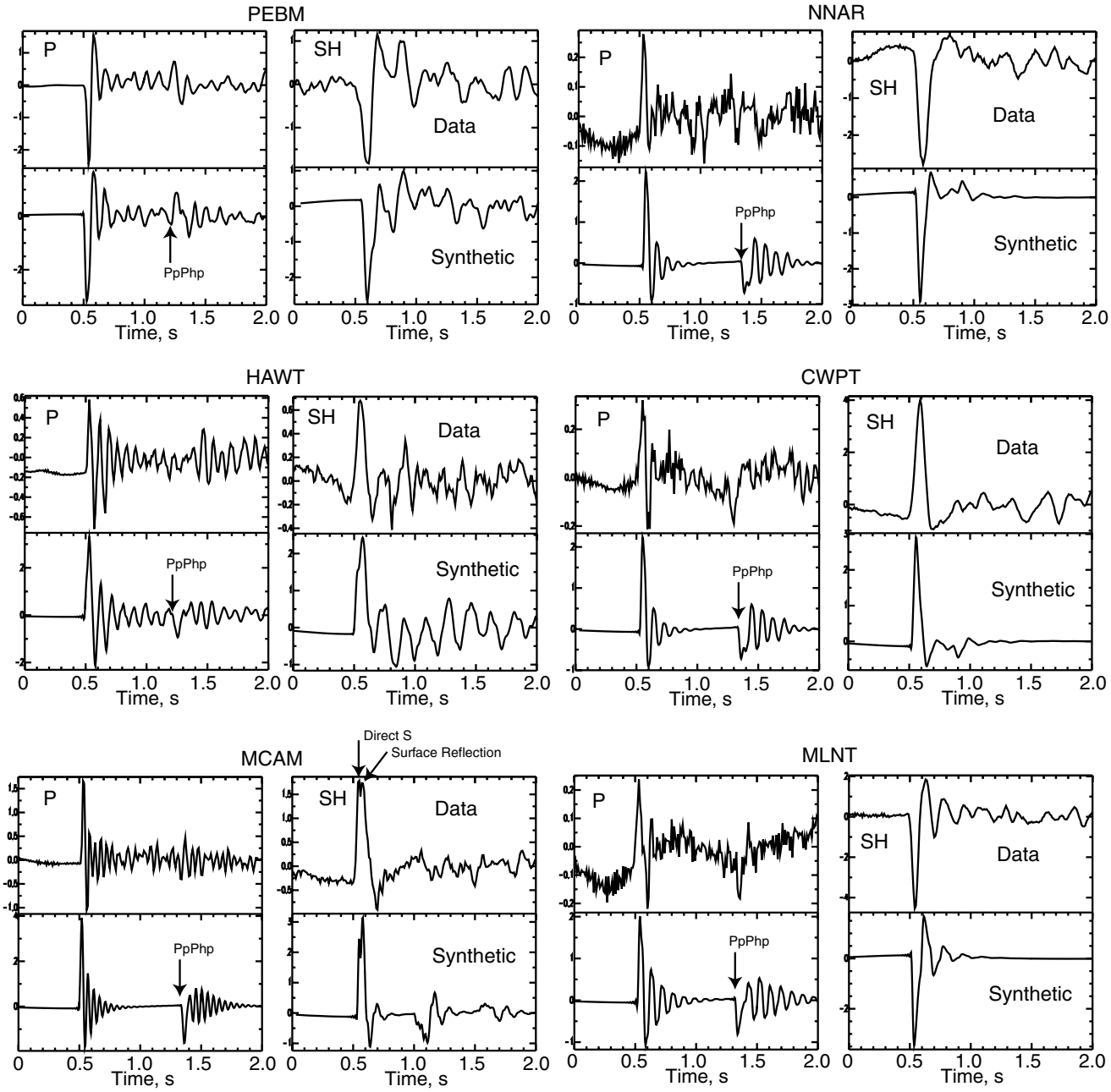

Figure 12. Comparison of data and synthetic waveforms for the events and stations of Figure 3. Models are listed in Table 5.

some complexity and amplitude to arrivals between the *P* and *PpPhp*, but the resonance induced by the near-surface layer dominates the waveform. The *SH*-wave response is more complicated. Clearly there is a resonance in the *S* waveform for the simple two-layer model, but this resonance beats against other near-surface reflections to produce a complicated *SH*-wave train after direct *SH*. The whole-sediment *S* multiple, *SsShs*, degrades significantly in multilayer models with or without the near-surface layer.

The complex 1000-layer velocity model was investigated in more detail to determine what portions of the model were contributing phases within the first 0.5 sec of the *S*-wave arrival. The bottom part of the model was replaced with a progressively thickened homogeneous layer with average sediment velocities. It was found that the *SH* waveform in this arrival time window was only sensitive to structure in the upper 60 m of the structure. Of course, the simpler structures progressively removed coda waves.

HAWT Structure

The Wilson 2-14 model was again used for modeling the *P* and *SH* waveforms at HAWT. Because the HAWT *P*

Table 5
Layered Earth Model Parameters

Station Code	V_p (m/sec)	V_s (m/sec)	Density (kg/m^3)	Thickness (m)
PEBM	510 over Wilson 2-14	250	1510	12.8
HAWT	300 over Wilson 2-14	150	1510	7.0
MCAM	500	200	1100	6.0
	2100	250	1900	60.0
	2100	600	1900	740.0
NNAR	700	350	1500	15.0
CWPT	2100	450	1900	60.0
	2100	600	1900	740.0
MLNT	450	250	1500	10.0
	2100	600	1900	800.0

waveform contained higher amplitude reverberations, an attempt was made to increase the velocity contrast of the surface layer while thinning it to preserve the higher frequency content of the reverberations (Table 5). Another complication was the requirement that the correct receiver depth be used for all stations. The L28 short-period stations are buried in shallow boreholes at 3 m depth. The effect of depth can be seen in the synthetic seismograms because the velocities are very low near the surface. The free-surface *P* or *S* reflection interferes with the direct wave causing pulse broadening.

The data/synthetic comparison of Figure 12 shows that it was difficult to reproduce the size of later *P* reverberations but that the resonance effect is clear. The *SH* waveform is quite complicated, showing a long coda that is mimicked by the model.

MCAM Structure

The *P* waveform recorded at MCAM shows the highest frequency reverberation response of any data examined here. The *SH* waveform also was one of the simplest seen at any station. Basically, the *SH* response of the Wilson 2-14 model with a near-surface layer looks like that shown for station HAWT. It always produces significant secondary arrivals due to a large low-velocity zone near the top of the model. It was concluded that this model is not appropriate for MCAM or for the other stations displaying simple *SH* waves, NNAR and CWPT. Thus, to keep the modeling simple, one- and two-layer models were investigated to model the *P* and *SH* waveforms. It was also found that the source function used for the other stations (a Brune pulse with 0.015-sec decay) was too broad and could not reproduce the high-frequency reverberation series seen in the data. Thus, a variety of source functions were tried trying to balance the width of the *S*-wave pulse against the clear high-frequency reverberations seen in the *P* waveform. A Brune pulse with a time decay of 0.01 sec was assumed in Figure 12.

The *P* waveform is dominated by high-frequency reverberations in the 6-m layer. Receiver depth was an important constraint since very low *P*-wave velocities ($v_p <$ 500 m/sec) caused significant pulse broadening in the first *P*-wave peak and degraded the reverberation series. The model also incorporates a lower density for the layer in an attempt to prolong the reverberation series in time.

The *SH* waveform is interesting in that it apparently shows the direct *S* wave and the free-surface reflection from above the buried seismometer. Again, the receiver depth gives a constraint on the velocity above the receiver through the arrival time of the observed reflection. However, the overall pulse width of the *S* wave is underestimated, which suggests unmodeled deeper structure, problems with the assumed source function, and assumed values of *Q* along the whole path.

These trade-offs among the source function, surface layer parameters, and deeper velocity model illustrate the difficulties in arriving at a unique model for structure at these stations. However, the synthetics demonstrate that near-surface structure is very important in shaping the principal aspects of the *P* and *S* waveforms.

NNAR and CWPT Structure

NNAR and CWPT waveforms show fewer large effects of near-surface structure in the *P* and *SH* waveforms compared to the other stations. Both stations were treated together and modeled by a single, relatively high velocity layer, over a layer with intermediate *S*-wave velocity (Table 5). The primary wave propagation effect occurs in the *P* waveforms where CWPT has a prominent backswing after the first *P* arrival. The backswing in the NNAR *P* wave is subdued. Again, the synthetic *S* waveforms appear to underestimate the width of the observed.

MLNT Structure

MLNT station data are included here because the nature of the *S* waveform is different than at the other stations. The *P* waveform data show at least two layer reverberations, but the *SH* waveform is distinctive and looks like a longer-period version of the *P* waveform at PEBM. Near-surface structure at MLNT can be approximated by a single layer-over-half-space model (Table 5) that reproduces the timing of *P*- and *S*-wave reverberations. Apparently, structure within the first 60 m of the surface is dominated by the surface layer response.

Discussion

There are many important implications in recognizing large site response wave propagation effects in the local earthquake data. These are concerned with determining velocity structure and source parameters, understanding anelastic attenuation, and ultimately, determining hazards due to strong ground motions.

It cannot be emphasized enough that there are significant trade-offs among the layer parameters and assumed source functions in the structure modeling for each station. However, the constraints on velocity by the Wilson 2-14

acoustic well log, observation of reverberation phases within the *P* and *S* waveforms, and the change in character of *P* and *S* waveforms between seismic stations all point to significant near-surface wave propagation effects that shape body-wave phases in the time and frequency domains. These observations are consistent with the variation of near-surface *P*- and *S*-wave velocities seen in detailed VSP well logs (Liu *et al.*, 1997), refraction studies (Street *et al.*, 2001), surface wave dispersion studies (Romero and Rix, 2001; Rix *et al.*, 2002), and geotechnical studies (Schneider *et al.*, 2001).

Clearly the earthquake data are sensitive to the media reflectivity. Refraction travel times or surface wave dispersion curves may tend to yield smooth velocity models. Shallow seismic reflection techniques may have the best chance of predicting *P*- and *S*-wave responses provided absolute wave velocities are suitably characterized. This would be a novel use of existing earthquake data to carefully analyze site responses for earthquake hazard evaluation. Notably, Williams *et al.* (2000) have applied small-scale reflection techniques to this problem with some success at sites in the Seattle, Washington, area and within the Mississippi embayment. They attempted to correlate resonance frequencies implied by the reflection models to whole-seismogram spectra from earthquake ground motions and observed clear spectral peaks corresponding to site resonance effects from structure in the upper 40 m.

It is clear that *P*- and *S*-wave site resonance and media scattering effects will mask the earthquake source function. Pulse-width measurements, for example, will be mainly a function of arrival time of the first *P*- or *S*-wave multiple in the layer. In the frequency domain resonance peaks will tend to bias corner frequency estimates (Williams and Langston, 1990). The synthetics of Figure 10a show that velocity heterogeneity within the sediment column is very important in broadening the *S*-wave pulse, even in the absence of clear near-surface-layer reverberations.

Broadening of pulses and spectral shaping by sediment reverberations bring up the issue of anelastic attenuation and how it is measured. It is interesting to note that all of the plane-layered models computed in the present study incorporated values of Q_p and Q_s of 500 and 250, respectively. This seems to fly in the face of most published *Q* determinations that have very low Q_p and Q_s for embayment sediments (e.g., $Q_p = 60$ and $Q_s = 30$ from Liu *et al.* [1994] and Chen *et al.* [1994]). Heterogeneous sediment models and near-surface layers go a long way in explaining relative *P*- and *S*-wave pulse widths and frequency content (Fig. 12). In fact, there is little direct evidence in these data for low *Q* values. Consider Figure 13, showing *P*/*SH* spectral ratios for high- and low-*Q* models at PEBM and MCAM along with observed spectral ratios. In the absence of earth structure effects, the *P*/*SH* spectral ratio should reflect differential attenuation between the *P* wave and *S* wave along the whole ray path. Since it is common to assume that *S* waves undergo more anelastic attenuation and that the *S* wave travels for a longer time along its ray path than the *P* wave, direct *S* should be depleted in higher frequency components compared to direct *P*. Figure 13 (and Fig. 7) shows that there is very little depletion of amplitude above the spectral peak near 12 Hz. The PEBM model with a Q_p of 500 and Q_s of 250 shows a *P*/*SH* ratio that is much higher than the data. Part of this is due to a *P*-wave resonance near 30 Hz, but most of the effect is due to depletion of high frequencies in the *S* wave due to the assumed anelasticity. Using proposed values of Q_p and Q_s of 60 and 30, respectively, produces a mismatch of 2–3 orders of magnitude between the observed ratio and synthetic ratio. The peak in the ratio near 12 Hz is due to a combination of resonance in the *P* wave and destructive interference in the *S* wave due to later arriving multiples.

Observed and theoretical *P*/*SH* spectral ratios are also shown for station MCAM. The data are contaminated by noise for frequencies greater than 30 Hz, and the *P*-wave resonance occurs near 20 Hz. The data show a broad peak between 10 and 20 Hz, which is approximately fit by the synthetic *P*/*SH* ratio for the high-*Q* model. However, the low-*Q* model shows a much greater depletion in high-fre-

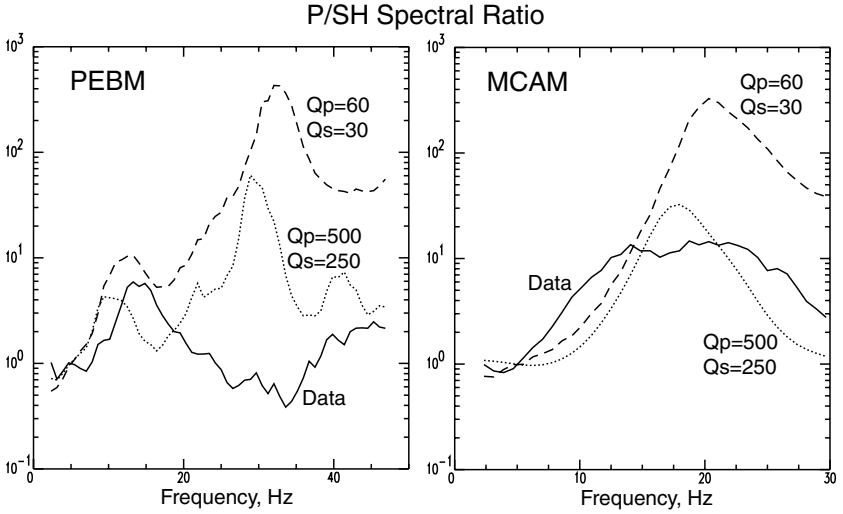

Figure 13. *P*/*SH* spectral ratios for PEBM (event 6) and MCAM (event 5). The same window and tapering parameters were used as used for the data in Figure 7. The solid curves show the observed *P*/*SH* ratio. Dotted curves are for the synthetics shown in Figure 12. $Q_p = 500$ and $Q_s = 250$ were assumed. The dashed curve shows spectral ratios for the same velocity models but assuming $Q_p = 60$ and $Q_s = 30$ after a suggestion made by Chen *et al.* (1994). There is no evidence in the observed spectral ratios for low *Q*.

quency amplitude for the *S* wave compared to *P* and is not consistent with the data.

Thus, it seems that even the high-*Q* model is not needed at PEBM to explain the observed *P*/*SH* wave ratio. The high-*Q* model is roughly consistent with the data at MCAM. In both cases, the low-*Q* model is not appropriate. This is a surprising result since it should be expected that anelastic attenuation will occur along the entire *P*- and *S*-wave ray path. This attenuation paradox is explored in greater detail in Langston (2003) through examination of the *Sp*/*S* spectral ratio method. The *Sp*/*S* spectral ratio data are seen to be biased by the same *P*- and *S*-wave site responses. The interaction of *P*- and *S*-wave spectral peaks produces spectral ratios that can be misinterpreted as an anelastic attenuation effect.

The data at PEBM allow a determination of average shear-wave velocity structure through the interpretation of *PpPhp*, *Ps*, *Sp*, and *S* arrival times. Well-log observations (Fig. 8) and experience with interpreting reflection data throughout the Mississippi embayment (R. Williams, personal comm., 2002) suggest that there are not significant variations in the bulk interval velocity for the unconsolidated sediments. Figure 12 shows that the first *P*-wave reverberation in the sediment layer has the correct travel time relative to direct *P* at PEBM. However, examination of *Ps* and *Sp* travel times on the horizontal components indicate that the *S*-wave velocity is generally too slow for the $n = 6$ velocity model (Fig. 14). A suite of velocity models was generated for differing values for the exponent, *n*, in equation (2). Synthetic seismograms were computed and compared to the observed waveform data in Figure 14. The relative times of *Ps*—*P* and *S*—*Sp* are sensitive functions of the average shear-wave velocity. A value of $n = 5.6$ fits these times best.

The average *P*- and *S*-wave slownesses for the $n = 5.6$ velocity model are 1.4395 and 0.4769, which give velocities of 2.10 and 0.695 km/sec, respectively. This gives a V_p/V_s ratio of 3.02 that implies an average Poisson's ratio of 0.44 that is not dependent on sediment thickness. The relative time of the first *P*-wave reverberation to the *Ps* conversion is a sensitive function of the V_p/V_s ratio. Assuming vertically incident waves for simplicity, the relative times of these phases can be manipulated to yield the V_p/V_s ratio independently of layer thickness:

$$\begin{aligned} t_{\mathrm{PpPhp}} - t_{\mathrm{P}} &= \frac{2h}{V_p}, \\ t_{\mathrm{Ps}} - t_{\mathrm{PpPhp}} &= \frac{h}{V_s} - \frac{3h}{V_p}, \\ \frac{V_p}{V_s} &= 2\left(\frac{t_{\mathrm{Ps}} - t_{\mathrm{PpPhp}}}{t_{\mathrm{PpPhp}} - t_p}\right) + 3. \end{aligned} \tag{5}$$

This is a robust method for determining Poisson's ratio in this area since the first *P*-wave reverberation and the *Ps* conversion are often seen. The data in Figure 3 show that *Ps* sometimes arrives shortly before *PpPhp* and sometimes shortly after, suggesting that the average V_p/V_s ratio is approximately 3. The velocity model for $n = 5.6$ is only slightly faster compared to the $n = 6$ velocity model shown in Figure 9, so it is not compared graphically. The greatest changes in shear-wave velocity occur near the surface where the porosity effect in equation (2) is greatest. V_p/V_s ratios are about 5.5–6 in the upper 50 m of the Wilson 2-14 model, decrease to ~3 for 500 m, and then decrease to ~2.4 in the lower part.

These average velocities are somewhat larger than those determined by Chen *et al.* (1996) in their study of *Sp* conversion times in the NMSZ. They assumed an average *P*-wave velocity of 1800 m/sec to derive the average *S*-wave velocity from differential *S*–*Sp* travel times. Increasing the average *P*-wave velocity to 2100 m/sec in their study would bring their results into agreement with the present *S*-wave velocity determination.

Conclusions

The effect of low-velocity, near-surface structure produces ubiquitous high-frequency (5–20 Hz) *P*- and *S*-wave site resonance in the local microearthquake data recorded on Mississippi embayment sediments. *P* and *S* waveforms display large secondary reverberations from structure in the upper 60 m and long-duration coda due to deeper velocity heterogeneity within the sedimentary section. Responses vary from site to site due to the variability of near-surface alluvium and suggest significant site amplification at these resonant frequencies. Site resonance explains the principal differences in frequency content between *P* and *S* waves and will affect source spectrum estimates if ignored. The *P*- and *S*-wave data do not show any direct evidence of significant anelasticity within embayment sediments. Near-surface resonance affects *P* and the converted *Sp* phase in a similar way, while *S* and *Ps* are also similar in their own way. This has important implications for *Q* estimates using these seismic phases.

The earthquake data show a variety of *P* and *S* body-wave phases that are set up by conversion at the sediment–basement boundary. In particular, the first sediment *P*-wave reverberation and *Ps* conversion times can be used to estimate the average sediment V_p/V_s ratio (3.02) and Poisson's ratio (0.44) independent of sediment thickness. A Nafe–Drake relation is developed to derive detailed shear-wave velocity from acoustic well logs. The exponent, *n*, for relating sediment shear-wave velocity from the porosity is seen to be equal to 5.6 for the embayment sediments of the central NMSZ.

Acknowledgments

I would like to thank Paul Bodin for many stimulating discussions concerning wave propagation in the Mississippi embayment and for use of his sediment thickness data shown in Figure 1, and, with Glenn Rix, for providing the Wilson 2–14 acoustic well-log data. Greg Steiner and Jim Bollwerk were indispensable in educating me on the installation, construction, and responses of stations of the CERI network. Mitch Withers provided the CERI network waveforms used in this study and helped configure my computer system to access the data directly. Jer-Ming Chiu is gratefully

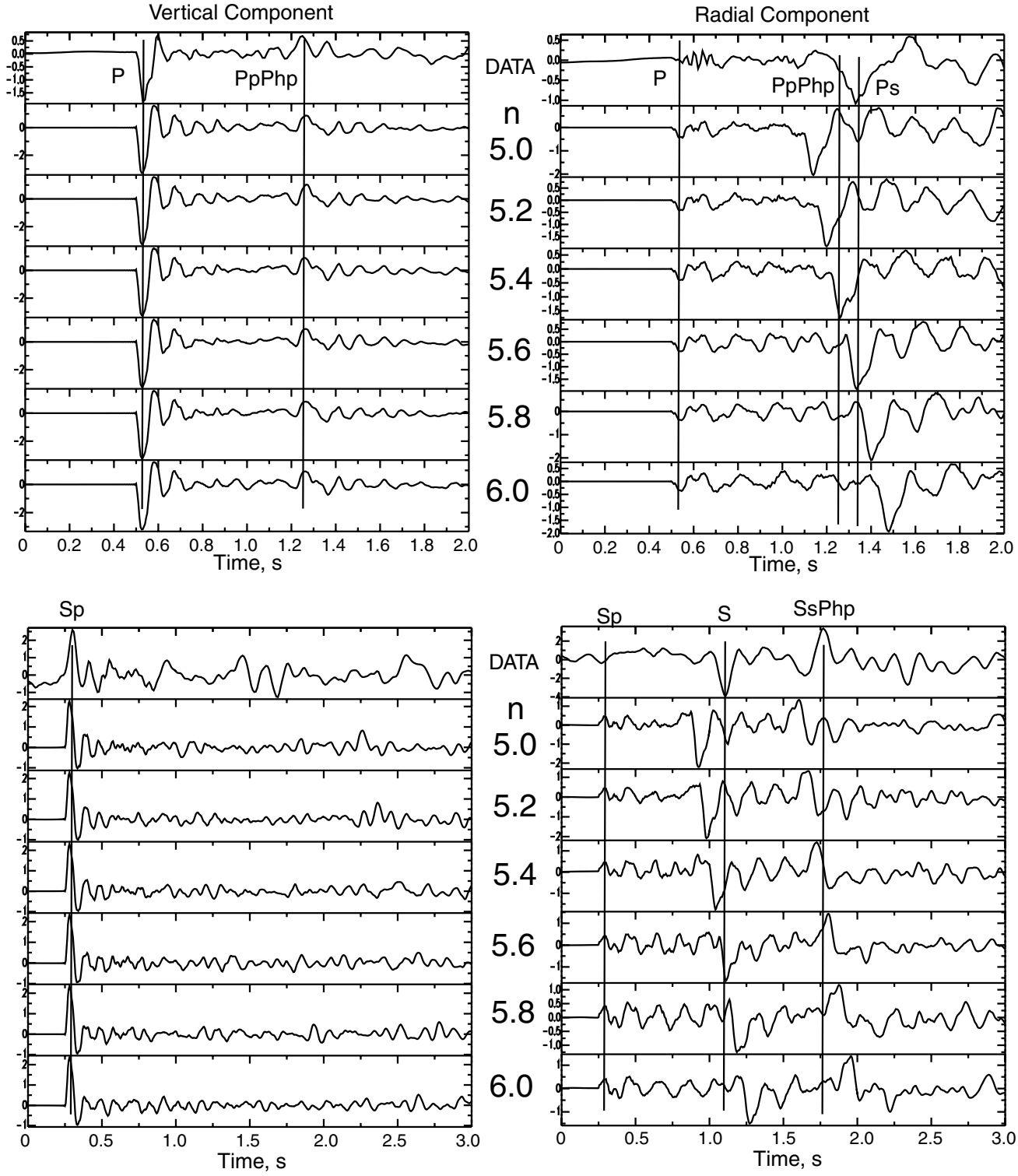

Figure 14. Comparison of synthetics constructed using various assumed values of n (equation 2) for PEBM station and the Wilson 2-14 velocity model. The relative times *PpPhp* and *Ps* constrain n to be 5.6.

acknowledged for providing digitized copies of the Haynes, Wilson, and Garigan well-log data. I would also like to thank Buddy Schweig and Rob Williams for useful comments and ideas on geologic structure and wave propagation in the Mississippi embayment. Use of the GMT program for Figure 1 (Wessel and Smith, 1998) is gratefully acknowledged. The Seismic Analysis Code (Goldstein *et al.*, 2002) was used for much of the analysis and plotting in this article. The manuscript was improved by comments made by an anonymous reviewer and Martin Chapman, the associate editor. This research was supported by the Center for Earthquake Research and Information while the author was a visitor, by the U.S. Department of Interior, U.S.G.S. NEHRP Grant 01HQGR0024, and by the Mid-America Earthquake Center under Grant HD-5. This is CERI Contribution Number 464.

References

Abercrombie, R. E. (1997). Near-surface attenuation and site effects from comparison of surface and deep borehole recordings, *Bull. Seism. Soc. Am.* **87,** 731–744.

Aki, K. (1988). Local site effects on strong ground motion, in *Earthquake Engineering and Soil Dynamics II: Recent Advances in Ground-Motion Evaluation*, J. L. V. Thun (Editor), American Society of Civil Engineers, Park City, Utah, 103–155.

Al-Shukri, H., and B. Mitchell (1990). Three-dimensional attenuation structure in and around the New Madrid seismic zone, *Bull. Seism. Soc. Am.* **80,** 615–632.

Al-Shukri, H., B. Mitchell, and H. A. A. Ghalib (1988). Attenuation of seismic waves in the New Madrid seismic zone, *Seism. Res. Lett.* **59,** 133–140.

Andrews, M. C., W. D. Mooney, and R. P. Meyer (1985). The relocation of microearthquakes in the northern Mississippi embayment, *J. Geophys. Res.* **90,** 10,223–10,236.

Apsel, R. (1979). Dynamic Green's functions for layered media and applications to boundary value problems, *Ph.D. Thesis*, University of California, San Diego.

Bath, M., and R. Stefansson (1966). *S-P* conversion at the base of the crust, *Ann. Geofis.* **19,** 119–130.

Bodin, P., K. Smith, S. Horton, and H. Hwang (2001). Microtremor observations of deep sediment resonance in metropolitan Memphis, Tennessee, *Eng. Geol.* **62,** 159–168.

Brune, J. N. (1970). Tectonic stress and the spectra of seismic shear waves from earthquakes, *J. Geophys. Res.* **75,** 4997–5009.

Catchings, R. D. (1999). Regional V_p, V_s, V_p/V_s and Poisson's ratios across earthquake source zones from Memphis, TN, to St. Louis, MO, *Bull. Seism. Soc. Am.* **89,** 1591–1605.

Chen, K., J. Chiu, and Y. Yang (1996). Shear-wave velocity of the sedimentary basin in the upper Mississippi embayment using *S*-to-*P* converted waves, *Bull. Seism. Soc. Am.* **86,** 848–856.

Chen, K.-C., J.-M. Chiu, and Y.-T. Yang (1994). Q_p-Q_s relations in the sedimentary basin of the Mississippi embayment using converted phases, *Bull. Seism. Soc. Am.* **84,** 1861–1868.

Chiu, J. M., A. C. Johnston, and Y. T. Yang (1992). Imaging the active faults of the central New Madrid seismic zone using Panda array data, *Seism. Res. Lett.* **63,** 375–393.

Chiu, J.-M., G. Steiner, J. R. Smalley, and A. C. Johnston (1991). PANDA: a simple, portable seismic array for local to regional scale seismic experiments, *Bull. Seism. Soc. Am.* **81,** 1000–1014.

Cong, L., J. Mejia, and B. J. Mitchell (2000). Attenuative dispersion of *P* waves in and near the New Madrid seismic zone, *Bull. Seism. Soc. Am.* **90,** 679–689.

Cramer, C. H. (1995). Weak-motion observations and modeling for the Turkey Flat, U.S., site-effects test area near Parkfield, California, *Bull. Seism. Soc. Am.* **85,** 440–451.

Crone, A. J. (1981). Sample description and stratigraphic correlation of the New Madrid test well 1-x, New Madrid County, Missouri, *U.S. Geological Survey Open File Report 81-426.*

Dorman, J., and R. Smalley (1994). Low-frequency seismic surface waves in the upper Mississippi embayment, *Seism. Res. Lett.* **65,** 137–148.

Futterman, W. I. (1962). Dispersive body waves, *J. Geophys. Res.* **67,** 5279–5291.

Gao, F. (1999). High-resolution upper crustal *P* and *S* velocity structures in the upper Mississippi embayment, *M.S. Thesis*, University of Memphis, Tennessee.

Ginzberg, A., W. D. Mooney, A. W. Walter, W. J. Lutter, and J. H. Healy (1983). Deep structure of northern Mississippi embayment, *Am. Assoc. Petrol. Geol.* **67,** 2031–2046.

Goldstein, P., and L. Minner (1996). SAC2000: seismic signal processing and analysis tools for the 21st century, *Seism. Res. Lett.* **67,** 39.

Goldstein, P., D. Dodge, and M. Firpo (2002). SAC2000: signal processing and analysis tools for seismologists and engineers, in *IASPEI International Handbook of Earthquake and Engineering Seismology*, Academic Press, San Diego.

Haskell, N. A. (1960). Crustal reflection of plane *SH* waves, *J. Geophys. Res.* **65,** 4147–4150.

Haskell, N. A. (1962). Crustal reflection of plane *P* and *SV* waves, *J. Geophys. Res.* **67,** 4751–4767.

Herrmann, R. B., and C. J. Ammon (1997). Faulting parameter of earthquakes in the New Madrid, Missouri, region, *Eng. Geol.* **46,** 299–311.

Hildenbrand, T. G., and J. D. Hendricks (1995). Geophysical setting of the Reelfoot rift and relations between rift structures and the New Madrid seismic zone, *U.S. Geolo. Surv. Profess. Pap. 1538-E*, 30 pp.

Johnston, A. C., and E. S. Schweig (1996). The enigma of the New Madrid earthquakes of 1811–1812, *Ann. Rev. Earth Planet. Sci.* **24,** 339–384.

Kang, I. B., and G. McMechan (1994). Separation of intrinsic and scattering *Q* based on frequency-dependent amplitudes of transmitted waves, *J. Geophys. Res.* **99,** 23,875–23,885.

Kind, R. (1978). The reflectivity method for a buried source, *J. Geophys.* **44,** 603–612.

Langston, C. A. (1994). An integrated study of crustal structure and regional wave propagation for southeastern Missouri, *Bull. Seism. Soc. Am.* **84,** 105–118.

Langston, C. A. (2003). Local earthquake wave propagation through Mississippi embayment sediments, Part II: Influence of local site velocity structure on Q_p-Q_s determinations, *Bull. Seism. Soc. Am.* **93,** 2685–2702.

Liu, H., Y. Hu, J. Dorman, T. Chang, and J. Chiu (1997). Upper Mississippi embayment shallow seismic velocities measured *in situ, Eng. Geol.* **46,** 313–330.

Liu, Z., M. E. Wuenscher, and R. B. Herrmann (1994). Attenuation of body waves in the central New Madrid seismic zone, *Bull. Seism. Soc. Am.* **84,** 1112–1122.

Mooney, W. D., M. C. Andrews, A. Ginzburg, D. A. Peters, and R. M. Hamilton (1983). Crustal structure of the northern Mississippi embayment and a comparison with other continental rift zones, *Tectonophysics* **94,** 327–348.

Moore, G. K., and D. L. Brown (1969). Stratigraphy of the Fort Pillow test well, Lauderdale County, Tennessee, Tennessee Department of Conservation, Division of Geology, Report of Investigations 26.

Nafe, J. E., and C. L. Drake (1957). Variation with depth in shallow and deep water marine sediments of porosity, density, and the velocities of compressional and shear waves, *Geophysics* **22,** 523–552.

Nelson, K. D., and J. Zhang (1991). A COCORP deep reflection profile across the buried Reelfoot rift, south-central United States, *Tectonophysics* **197,** 271–293.

Nuttli, O. W. (1973). The Mississippi Valley earthquakes of 1811 and 1812: intensities, ground motions, and magnitudes, *Bull. Seism. Soc. Am.* **63,** 227–248.

Pujol, J., S. Pezeshk, Y. Zhang, and C. Zhao (2002). Unexpected values of Q_s in the unconsolidated sediments of the Mississippi embayment, *Bull. Seism. Soc. Am.* **92,** 1117–1128.

Rix, G. J., G. L. Hebeler, and M. C. Orozco (2002). Near-surface V_s profiling in the New Madrid Seismic Zone using surface-wave methods, *Seism. Res. Lett.* **73,** 380–392.

Romero, S., and G. J. Rix (2001). Regional variations in near surface shear wave velocity in the greater Memphis area, *Eng. Geol.* **62,** 137–158.

Schneider, J. A., P. W. Mayne, and G. J. Rix (2001). Geotechnical site characterization in the greater Memphis area using cone penetration tests, *Eng. Geol.* **62,** 169–184.

Schwab, F., and L. Knopoff (1973). Love wave dispersion computations, *Bull. Seism. Soc. Am.* **63,** 1107–1117.

Seale, S. H., and R. J. Archuleta (1989). Site amplification and attenuation of strong ground motion, *Bull. Seism. Soc. Am.* **89,** 1673–1696.

Self, R. P. (1993). Late Tertiary to early Quaternary sedimentation in the Gulf coastal plain and lower Mississippi valley, *Southeast. Geol.* **33,** 99–110.

Stearns, R. G. (1957). Cretaceous, Paleocene, and lower Eocene geologic history of the northern Mississippi embayment, *Geol. Soc. Am. Bull.* **68,** 1077–1100.

Stearns, R. G., and M. V. Marcher (1962). Late Cretaceous and subsequent structural development of the northern Mississippi embayment area, *Geol. Soc. Am. Bull.* **73,** 1387–1394.

Street, R., E. W. Woolery, Z. Wang, and J. B. Harris (2001). NEHRP soil classifications for estimating site-dependent seismic coefficients in the upper Mississippi embayment, *Eng. Geol.* **62,** 123–135.

VanArsdale, R. B., and R. K. TenBrink (2000). Late Cretaceous and Cenozoic geology of the New Madrid seismic zone, *Bull. Seism. Soc. Am.* **90,** 345–356.

Vlahovic, G., C. Powell, and J. Chiu (2000). Three-dimensional *P* wave velocity structure in the New Madrid seismic zone, *J. Geophys. Res.* **105,** 7999–8012.

Wang, Z., R. Street, E. Woolery, and J. Harris (1994). Q_s estimation for unconsolidated sediments using first-arrival *SH* wave critical refractions, *J. Geophys. Res.* **99,** 13,543–13,551.

Wessel, P., and W. H. F. Smith (1998). New, improved version of Generic Mapping Tools released, *EOS* **79,** 579.

Williams, D. E., and C. A. Langston (1990). Observational test for wave propagation effects in local earthquake seismograms, *Seism. Res. Lett.* **61,** 109–116.

Williams, R. A., W. J. Stephenson, A. D. Frankel, E. Cranswick, M. E. Meremonte, and J. K. Odum (2000). Correlation of 1- to 10-Hz earthquake resonances with surface measurements of *S*-wave reflections and refractions in the upper 50 m, *Bull. Seism. Soc. Am.* **90,** 1323–1331.

Center for Earthquake Research and Information
University of Memphis
3876 Central Avenue, Suite 1
Memphis, Tennessee 38152

Manuscript received 11 March 2003.